Performance Analysis of Current Control Strategies for Hybrid Stepper Motors

FABio BERNARDI [1] (Student Member, IEEE), **EMILIO CARFAGNA** [1] (Student Member, IEEE),
GIOVANNI MIGLIAZZA [1] (Member, IEEE), **GIAMPAOLO BUTICCHI** [2] (Senior Member, IEEE),
FABIO IMMOVILLI [1] (Senior Member, IEEE), **AND EMILIO LORENZANI** [1] (Senior Member, IEEE)

[1]Department of Sciences and Methods for Engineering, University of Modena and Reggio Emilia, 42122 Reggio Emilia, Italy
[2]Zhejiang Key Laboratory on the More Electric Aircraft Technologies, University of Nottingham Ningbo China, Ningbo 315100, China

CORRESPONDING AUTHOR: GIAMPAOLO BUTICCHI (e-mail: buticchi@ieee.org)

ABSTRACT Hybrid stepper motors are widespread in industrial automation due to their robustness and high torque performance in low speed range, e.g. 3D printers, pick and place, and generally in many low power positioning applications. In order to increase the efficiency and dynamic performance, current/speed/position closed loop controls are implemented for high performance sensored stepper drives. The main challenge comes from the high number of magnetic poles which these motors feature, increasing the ratio between the fundamental and switching frequency. This paper critically evaluates four current control structures based field oriented control: classic PI regulators, sliding mode control, deadbeat predictive current control and model predictive current control. Simulations and experimental results aim to evaluate the dynamic performance, phase current amplitude and distortion in order to support the critical comparison.

INDEX TERMS Hybrid stepper motor, PI control, sliding mode control, deadbeat predictive current control, model predictive current control.

I. INTRODUCTION

The hybrid stepper motors (HSMs) are widely adopted in industrial and consumer applications thanks to their low cost, high reliability and the possibility of being easily controlled in open-loop position control. However, the main drawbacks of the open-loop control are the low motor efficiency due to the high copper loss at partial load conditions and the possibility of stalling for high values of the load torque. Although modifications of the open-loop control, such as the microstepping method, allows obtaining a smoother behaviour [1], the efficiency is strongly load dependent. For these reasons, closed loop controls such as field oriented control (FOC) are thus natural candidates to improve performance, efficiency and robustness with respect to microstepping control [2]. However, the linear control stability gets challenged for low ratios of switching frequency f_{sw} to electrical frequency, i.e f_{sw}/f_{el}, so the switching frequency has to be increased to prevent unstable behaviours.

Relevant contributions in literature when mechanical quantities are measured can be found in [3], which compares adaptive learning and repetitive learning controls for position reference profiles that are periodic signals with known period, whereas [4] proposes the minimization of the cogging torque and [5] addresses the position-tracking problem. The purpose of this paper is to analyze the performance of FOC, sliding mode control (SMC) adopted in [6] for a PMSM using a sign function which guarantees the stability and induces a sliding motion on the surface, deadbeat predictive current control (DPCC), used in [7] for a permanent magnet synchronous machine and extended as Dahlin controller in [8], and model predictive control (MPC), used in [9] with its finite control set model predictive control (FCS-MPC) variant. Model predictive controls, in fact, offer the possibility to reduce the effective switching frequency of the converter while maintaining fast dynamic response, with a simple inclusion of multiple objectives and constraints without introducing extra control loops. In addition, FCS-MPC was recently proposed for high performance control of AC drives [10] even in case of thermal control [11] and multilevel converters [12].

The performance of the different control strategies will be compared in terms of current-loop bandwidth, step response, root mean square value (RMS) and total harmonic distortion (THD) of the phase currents.

This manuscript fills a gap in the existing literature, showing a critical evaluation, supported by extensive experimental results, of the different possibilities for FOC in hybrid stepper motors. The paper is organized as follows: Section II describes the adopted mathematical model of HSM, Section II-A highlights some critical issue related to the use of a Digital signal Processor (DSP) in the design of the control strategies, Section III reports the proposed current control architectures (PI control, SMC, DPCC, MPC), while Section IV and Section V include simulation and experimental results, followed by Conclusions.

II. MATHEMATICAL MODEL

The dynamic of a two phase hybrid stepper motor in the (d, q) reference frame, according to [13], is given by:

$$
\begin{cases}
u_d = L_0 \frac{di_d}{dt} + R_s i_d - i_q N_r \omega L_0 \\
u_q = L_0 \frac{di_q}{dt} + R_s i_q + i_d N_r \omega L_0 + k_M \omega \\
\dot{\theta} = \omega \\
J\dot{\omega} + F\omega = T_e - T_L - T_c \\
T_e = k_M i_q \\
T_c = N_r F_m^2 \sum_{j=1}^{m} 4jP_{4j} \sin(4jN_r\theta)
\end{cases}
\tag{1}
$$

where: θ is the (mechanical) rotor angle, ω is the (mechanical) rotor speed, (i_d, i_q) are the stator currents and (u_d, u_q) are the stator voltages. The variables $(\theta, \omega, i_d, i_q)$ are the state variables, while (u_d, u_q) are the control inputs and the load torque T_L is the unknown disturbance input.

The other model parameters are: the viscous friction coefficient F, the number of rotor teeth N_r, the moment of inertia J, the stator winding resistance R_s, the stator inductance L_0 and the torque constant k_M equal to $N_r\phi_{PM}$ where ϕ_{PM} is the flux linkage provided by the permanent magnet.

The term T_e is the electromagnetic torque produced by the motor and T_c models the disturbance torque due to cogging (F_m is the magneto-motive force of permanent magnet and P_{4j} is the amplitude of the j harmonics as stated by [14]). The electrical speed and angle are $\omega_e = N_r\omega$ and $\theta_e = N_r\theta$, respectively.

The derivation of the model above is obtained under the assumptions that self and mutual inductance of the two windings are constant with respect to θ.

A. MODELLING OF THE DELAY EFFECTS

Fig. 1 shows the typical time sequence associated with the state variables sampling, computation and PWM updating, where T_s is the sampling period.

During a switching cycle N, the stator currents (i_α, i_β) and the rotor angle θ are sampled. At the same time, considering e.g. the period from time T_k to T_{k+1}, the DSP performs the
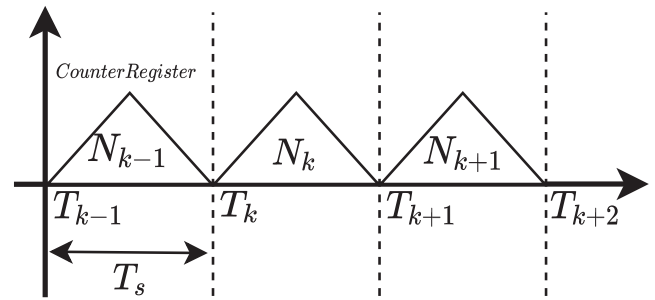

FIGURE 1. Time sequence of state variables sampling and PWM update.

updating of the PWM of the $N_{k-1_{th}}$ cycle and the calculation of the PWM of the $N_{k_{th}}$ cycle.

It can be observed that the PWM update of the previous cycle N_{k-1} involves a processing time delay. Since the counting period is fixed to one switching period T_s, this delay corresponds exactly to T_s and it has been included in the control design in order to obtain more realistic simulations.

In the same way, the rotor position is read at the $N_{k_{th}}$ cycle while the control voltages of the different topologies are applied at the $N_{k+1_{th}}$ cycle. In order to solve this problem a rotor position compensation has been adopted.

According to [15], after a switching period T_s the PWM of the $N_{k-1_{th}}$ cycle is updated, but the actual output voltage V_{act} activates from T_s to $2T_s$.

Following the volt-second principle in [15], the relationship between the actual voltage V_{act} and the original voltage output by current regulator V_{ori} results as:

$$
\begin{aligned}
V_{act} &= \frac{1}{T_s} \int_{T_s}^{2T_s} e^{j\omega_e\tau} V_{ori} dt \\
&= \frac{2}{\omega_e T_s} \sin\left(\frac{\omega_e T_s}{2}\right) e^{j\omega_e T_s} V_{ori}
\end{aligned}
\tag{2}
$$

According to (2), V_{act} is delayed of $1.5T_s$ due to delayed PWM. The delay angle $\Delta\theta$ is therefore expressed as:

$$
\Delta\theta = 1.5 N_r \omega T_s
\tag{3}
$$

The rotor position compensation is adopted for each control strategy by adding $\Delta\theta$ to the electrical rotor angle θ_e when the inverse Park transformation is computed.

III. DESCRIPTION OF THE CONTROL STRATEGIES

The current control schemes adopted in this paper are described in this section. The power circuit of the dual H-bridge inverter feeding the HSM is reported in Fig. 2.

This converter topology consists of a dual H-bridge inverters supplied by the same DC voltage but feeding the two windings of the HSM independently. Technical details about the different control strategies are provided in the following subsections.

A. PROPORTIONAL-INTEGRAL CONTROL

The PI control scheme is reported in Fig. 3.
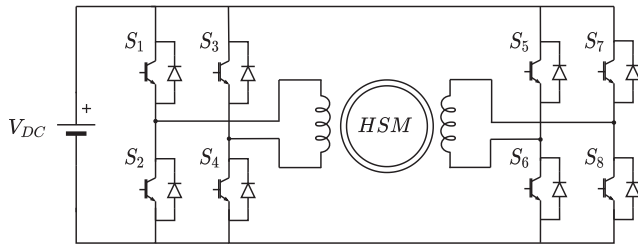
FIGURE 2. Power circuit of the dual H-bridge inverter feeding the HSM.
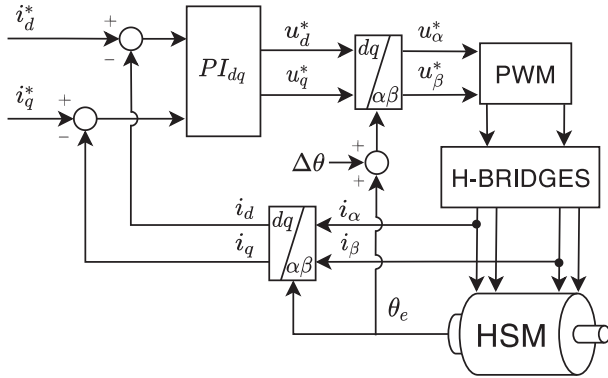
FIGURE 3. PI control scheme.
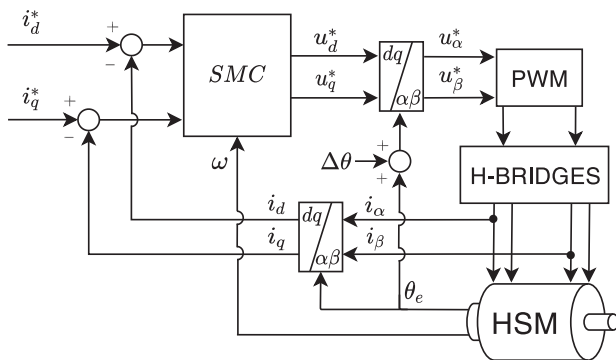
FIGURE 4. Sliding mode control scheme.

In order to prevent that the integral part of the PI control "winds-up," the back-calculation strategy has been implemented as described in [16] and the Tustin transform has been used to convert the PI regulators to the discrete domain.

Parameters are tuned following closed-loop Ziegler-Nichols method.

B. SLIDING MODE CONTROL

Sliding mode control scheme is reported in Fig. 4.

Sliding mode control has been widely applied in recent years for motor drive applications with speed/current control loops [6], [17] and with sensorless control [18], [19].

Defining the tracking error as $e_q = i_q^\star - i_q$, where $i_q^\star$ is the current reference and i_q is the measured current, the purpose is

to achieve e_q equal to 0. Let the sliding surface function equal to

$$\sigma_q = e_q + K_i \int e_q \qquad (4)$$

with K_i positive constant that determines the decay rate of the q-axis stator current error.

To guarantee that σ_q approaches zero in a finite time, a Lyapunov function $V = 0.5 \, \sigma_q^2$ is selected to induce $\sigma_q = 0$.

A common criterion is to achieve [20]

$$\dot{V} < -\gamma \, |\sigma_q| \qquad (5)$$

Taking the derivative of the sliding surface respect to time gives

$$\dot{\sigma}_q = \frac{d}{dt} i_q^\star - s i_q + K_i e_q$$
$$= \frac{d}{dt} i_q^\star - \frac{1}{L_0} u_q + \frac{R_s}{L_0} i_q + \frac{k_M}{L_0} \omega + p\omega i_d + K_i e_q \qquad (6)$$

Choosing u_q equal to

$$u_q = L_0 \left(\frac{d}{dt} i_q^\star + \frac{R_s}{L_0} i_q + \frac{k_M}{L_0} \omega + p\omega i_d + K_i e_q + k_q \mathrm{sgn}(\sigma_q) \right) \qquad (7)$$

The term k_q is selected in order to guarantee the stability even in case of wrong knowledge of the parameters, so considering ΔR_s, ΔL_0 and Δk_M as variations of the nominal parameters and assuming that $|\Delta R_s| < a$, $|\Delta L_0| < b$ and $|\Delta k_M| < c$, with a, b and c positive constant it is necessary to ensure that

$$k_q > \frac{1}{L_0} \left(b \left| \frac{d}{dt} i_q^\star \right| + a|i_q| + c|\omega| + pb|\omega||i_d| \right) \qquad (8)$$

then

$$\dot{V} = \dot{\sigma}_q \sigma_q$$
$$= -\gamma_q |\sigma_q| < 0 \qquad (9)$$

with $\gamma_q = k_q - 1/L_0(b \left| \frac{d}{dt} i_q^\star \right| + a|i_q| + c|\omega| + pb|\omega||i_d|)$.

In the same way, a control law for the d-axis voltage is derived as

$$u_d = L_0 \left(\frac{d}{dt} i_d^\star + \frac{R_s}{L_0} i_d - p\omega i_q + K_i e_d + k_d \mathrm{sgn}(\sigma_d) \right) \qquad (10)$$

where e_d is the tracking error equal to $i_d^\star - i_d$ and σ_d is the sliding surface equal to $e_d + K_i \int e_d$ with $k_d > \frac{1}{L_0} \left(b \left| \frac{d}{dt} i_d^\star \right| + a|i_d| + pb|\omega||i_q| \right)$.

As noted in [21] fast dynamics in the control loop, which were neglected in the system model, can be excited by the fast switching of sliding mode controllers. Moreover, digital implementations in microcontrollers with fixed sampling rates may lead to discretization chatter. This phenomenon is known as chattering and it has been verified that a sigmoidal function instead of the sign function can suppress this issue [18] when sliding mode observers (SMO) are used. In this case,
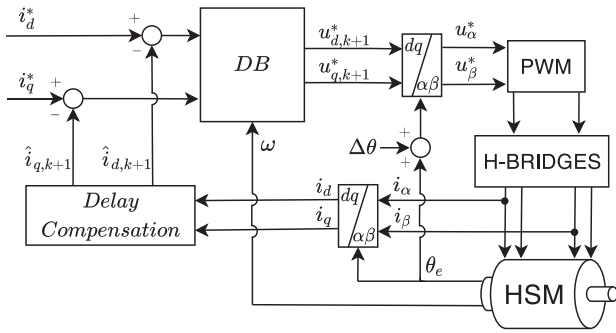
FIGURE 5. Deadbeat predictive current control scheme.

for current control the sign in (7) and (10) is replaced by the functions

$$
\begin{cases}
\dfrac{2k_d}{1 + \exp(-\alpha\sigma_d)} - 1 \\[2ex]
\dfrac{2k_q}{1 + \exp(-\alpha\sigma_q)} - 1
\end{cases}
\tag{11}
$$

C. DEADBEAT PREDICTIVE CURRENT CONTROL

Deadbeat predictive current control (DPCC) scheme is reported in Fig. 5. According to the deadbeat theory, by discretizing, the voltage vector required to obtain the desired stator current vector $i_{dq}^*(k)$ can be computed at the $(k + 1)_{th}$ sampling instant.

The electrical machine model can be discretized and approximated thanks to Euler's forward difference quotient

$$
\frac{di(t)}{dt} \approx \frac{i_{k+1} - i_k}{T_s}
\tag{12}
$$

The discrete voltage vectors are obtained from (1), considering that the currents at the $(k + 1)_{th}$ sampling instant are equal to the reference currents $i_{dq,k}^* = i_{dq,k+1}$

$$
u_{d,k} = L_0 \frac{i_{d,k}^* - i_{d,k}}{T_s} + R_s i_{d,k} - i_{q,k} N_r \omega_k L_0
$$

$$
u_{q,k} = L_0 \frac{i_{q,k}^* - i_{q,k}}{T_s} + R_s i_{q,k} + i_{d,k} N_r \omega_k L_0 + k_M \omega_k
\tag{13}
$$

In the ideal case, DPCC establishes a zero current error within one sampling interval T_s, but since a DSP is used to implement the algorithm, the DPCC voltage vectors computation causes an inherent calculation delay. Neglecting this delay leads to a persistent oscillation in the current control loop [22]. Moreover, the more accurate deadbeat control presented in [22] has a strong dependence on the knowledge of the electrical parameters, so the adopted deadbeat current control is based on [23] and the main equations are briefly reported. The parameter mismatches lead to steady state error between the stator current. The incremental model based deadbeat predictive current control (IDPCC) method adopted in [7], [23] has been adopted in order to achieve a zero steady state error eliminating the dependency from the permanent magnet flux linkage term.

Since the voltage equations at the k_{th} instant are computed as in (13), similarly the voltage equations at $(k - 1)_{th}$ sampling interval can be expressed by

$$
u_{d,k-1} = L_0 \frac{i_{d,k} - i_{d,k-1}}{T_s} + R_s i_{d,k-1} - i_{q,k-1} N_r \omega_{k-1} L_0
$$

$$
u_{q,k-1} = L_0 \frac{i_{q,k} - i_{q,k-1}}{T_s} + R_s i_{q,k-1} + i_{d,k-1} N_r \omega_{k-1} L_0
$$
$$
+ k_M \omega_{k-1}
\tag{14}
$$

Subtracting (14) from (13), the incremental prediction model is obtained under the assumption that the mechanical dynamics are much slower than electrical dynamics, so the rotor speed is considered constant (i.e. $\omega_k - \omega_{k-1} \approx 0$) during successive sampling periods:

$$
u_{d,k} = \frac{L_0}{T_s} i_{d,k+1} - \left(\frac{2L_0}{T_s} - Rs\right) i_{d,k} + \left(\frac{L_0}{T_s} - Rs\right) i_{d,k-1}
$$
$$
- \Delta i_{q,k} N_r \omega_k L_0 + u_{d,k-1}
$$

$$
u_{q,k} = \frac{L_0}{T_s} i_{q,k+1} - \left(\frac{2L_0}{T_s} - Rs\right) i_{q,k} + \left(\frac{L_0}{T_s} - Rs\right) i_{q,k-1}
$$
$$
+ \Delta i_{d,k} N_r \omega_k L_0 + u_{q,k-1}
\tag{15}
$$

It can be noted from (15) that the torque constant in the incremental predictive model is eliminated.

In order to compensate the computation delay due to the use of a DSP, the predicted current at the $(k + 1)_{th}$ sampling interval can be expressed as

$$
\hat{i}_{d,k+1} = \left(2 - \frac{T_s R_s}{L_0}\right) i_{d,k} - \left(1 - \frac{T_s R_s}{L_0}\right) i_{d,k-1}
$$
$$
+ \Delta i_{q,k} N_r \omega_k T_s + \Delta u_{d,k} \frac{T_s}{L_0}
$$

$$
\hat{i}_{d,k+1} = \left(2 - \frac{T_s R_s}{L_0}\right) i_{q,k} - \left(1 - \frac{T_s R_s}{L_0}\right) i_{q,k-1}
$$
$$
- \Delta i_{d,k} N_r \omega_k T_s + \Delta u_{d,k} \frac{T_s}{L_0}
\tag{16}
$$

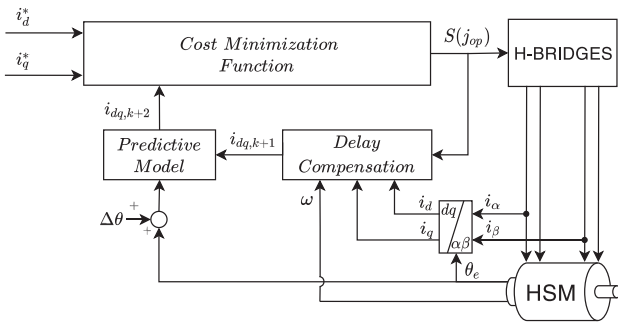where $\Delta i_{dq,k} = i_{dq,k} - i_{dq,k-1}$, $\Delta u_{dq,k} = u_{dq,k} - u_{dq,k-1}$.

Hence, the reference voltage at the $(k + 1)_{th}$ sampling interval can be obtained as

$$
u_{d,k+1}^* = \frac{L_0}{T_s} i_{d,k}^* - \left(\frac{2L_0}{T_s} - Rs\right) \hat{i}_{d,k+1} + \left(\frac{L_0}{T_s} - Rs\right) i_{d,k}
$$
$$
- \Delta i_{q,k+1} N_r \omega_k L_0 + u_{d,k}
$$

$$
u_{q,k+1}^* = \frac{L_0}{T_s} i_{q,k}^* - \left(\frac{2L_0}{T_s} - Rs\right) \hat{i}_{q,k+1} + \left(\frac{L_0}{T_s} - Rs\right) i_{q,k}
$$
$$
+ \Delta i_{d,k+1} N_r \omega_k L_0 + u_{q,k}
\tag{17}
$$

where $\Delta i_{dq,k+1} = i_{dq,k+1} - i_{dq,k}$.

D. MODEL PREDICTIVE CURRENT CONTROL

The FCS-MPC control scheme is reported in Fig. 6.

FIGURE 6. MPC control scheme.

Based on the current sampling states and the HSM model, a prediction of the machine currents is performed according to the length of the prediction horizon (equal to 1) with respect to all the 16 combinations of feasible voltage vectors related to the 2 H-Bridge inverter (every H-Bridge has 4 configurations that can be applied).

Assuming the same approximation reported in (12), the expression of the predicted currents i_{dq}, first available at the $(k+1)_{th}$ sampling interval, can be determined as
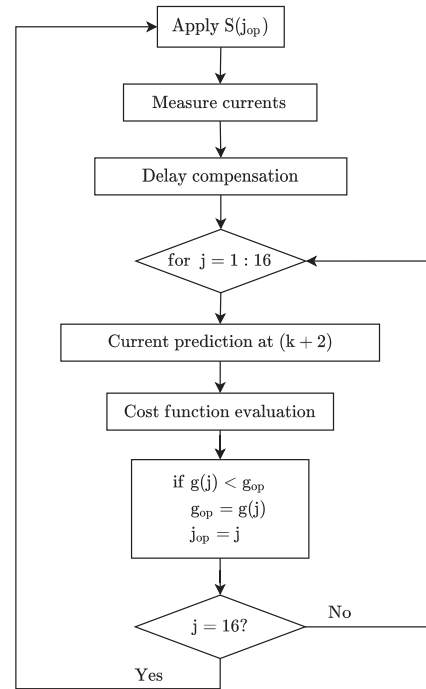
$$i_{d,k+1} = \left(1 - \frac{T_s R_s}{L_0}\right) i_{d,k} + i_{q,k} N_r \omega_k T_s + \frac{u_{d,k} T_s}{L_0}$$

$$i_{q,k+1} = \left(1 - \frac{T_s R_s}{L_0}\right) i_{q,k} - i_{d,k} N_r \omega_k T_s + \frac{u_{q,k} T_s}{L_0}$$

$$- \frac{k_M \omega_k T_s}{L_0} \tag{18}$$

The incremental model predictive current control model used in [24] has been adopted in order to improve the parameter robustness respect to the errors of the flux linkage provided by the permanent magnet. Since the predictive currents at the $(k+1)_{th}$ sampling interval can be predicted according to (18), similarly the currents at the k_{th} instant are expressed by

$$i_{d,k} = \left(1 - \frac{T_s R_s}{L_0}\right) i_{d,k-1} + i_{q,k-1} N_r \omega_{k-1} T_s + \frac{u_{d,k-1} T_s}{L_0}$$

$$i_{q,k} = \left(1 - \frac{T_s R_s}{L_0}\right) i_{q,k-1} - i_{d,k-1} N_r \omega_{k-1} T_s + \frac{u_{q,k-1} T_s}{L_0}$$

$$- \frac{k_M \omega_{k-1} T_s}{L_0} \tag{19}$$

Subtracting (19) from (18), the incremental prediction model is obtained as in (16). Since a microprocessor is used, depending on its sampling frequency and its speed, the time between the measurement of the load currents and the application of the next switching state can be considerable. If the difference between the computation time and the sampling time is significant, a time delay will negatively affect the performance of the system. In order to compensate for this delay, the solution proposed in [25] has been adopted.

The measured currents and the applied switching state at the sample instant k are used in (18) in order to estimate the value

FIGURE 7. Flow diagram of the implemented MPC algorithm.

of the load currents $i_{dq,k+1}$. Then, in order to compensate the delay, these predictions are used to compute the new current vectors, first available at the $(k+2)_{th}$ sampling instant.

$$i_{d,k+2} = \left(2 - \frac{T_s R_s}{L_0}\right) i_{d,k+1} - \left(1 - \frac{T_s R_s}{L_0}\right) i_{d,k}$$

$$+ \Delta i_{q,k+1} N_r \omega_k T_s + \Delta u_{d,k+1} \frac{T_s}{L_0}$$

$$i_{d,k+2} = \left(2 - \frac{T_s R_s}{L_0}\right) i_{q,k+1} - \left(1 - \frac{T_s R_s}{L_0}\right) i_{q,k}$$

$$- \Delta i_{d,k+1} N_r \omega_k T_s + \Delta u_{q,k+1} \frac{T_s}{L_0} \tag{20}$$

where $\Delta i_{dq,k+1} = i_{dq,k+1} - i_{dq,k}$, $\Delta u_{dq,k+1} = u_{dq,k+1} - u_{dq,k}$. In the proposed algorithm, depicted in Fig. 7, the predicted currents reported in (20) are evaluated by a cost function for each of the 16 combinations. The voltage vector whose current prediction is closest to the expected current reference is chosen and applied at the next sampling instant. In other words, the selected vector is the one that minimizes the cost function.

Since the computation associated to the MPC algorithm takes time to be completed, the computed new output voltage V_{act} activates after T_s. On the basis of this assumption, the delay angle adopted in the MPC strategy is changed in

$$\Delta \theta = N_r \omega T_s \tag{21}$$

According to [26], different cost functions can be chosen depending on the application. In accordance with the most common approaches, a quadratic cost function has been

TABLE 1. HSM Nameplate Parameters

Parameter	Symbol	Value	Unit
Nominal phase current	I_N	10	A_{pk}
Rotor teeth	N_r	50	-
Stator resistance	R_s	0.187	Ω
Stator inductance	L_0	1.63	mH
Torque constant	k_M	0.645	Nm/A
Nominal torque	T_L	5.2	Nm
Nominal speed	ω_N	100	rad/s

TABLE 2. H-Bridge Parameters

Parameter	Symbol	Value	Unit
DC link voltage	V_{dc}	70	V
PI, SMC and DPCC sampling frequency	f_s	20	kHz
MPC sampling frequency	f_s	40	kHz

chosen

$$g = \left(i_{d,k}^* - i_{d,k+2} \right)^2 + \left(i_{q,k}^* - i_{q,k+2} \right)^2 \qquad (22)$$

IV. SIMULATION RESULTS

The modeling and simulation of the different control techniques discussed in the previous section were carried out using Simulink/PLECS environments for a commercial AM34SS3DGA-N stepper motor.

In order to compare the control strategies, the machine dynamic model (see Table 1 for nameplate data) and the model of the two H-Bridges (see Table 2 for converter data) are kept the same throughout all simulations. The adopted modulation scheme for the PI control, SMC and the DPCC control is the unipolar PWM, while no modulator is needed for the MPC.

Although the switching frequency f_{sw} coincides with the sampling frequency f_s when considering PI, SMC and DPCC control, the MPC strategy behaves differently.

In [9] it is shown that the switching frequency for the MPC is variable and limited. In fact, the switching state of the inverter can be changed only once during each sampling instant T_s, thus the maximum switching frequency of the output voltages is limited to half of the sampling frequency f_s. It is worth mentioning that having a variable switching frequency could cause the current harmonics to fall within the audible spectrum, which is can be a disadvantage for certain applications, whereas it can be accepted for industrial plant usages. However, the switching states do not change every T_s if the same optimal state is selected, then the average switching frequency is always lower than $f_s/2$.

For example, in [26] it is demonstrated that increasing T_s five-fold, the switching frequency decreases by approximately five-fold and the total harmonic distortion (THD) increases five-fold. According to these considerations, to compare the performance of the different control strategies, it has been decided to double the MPC sampling frequency, although this choice leads the MPC strategy to exhibit an effective switching frequency f_{sw} that is lower than the PI, SMC and DPCC switching frequencies.
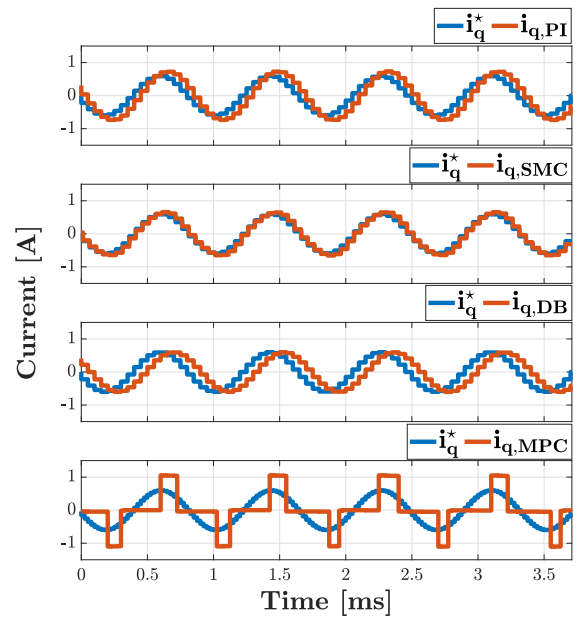

FIGURE 8. Response to a sinusoidal input with amplitude of 0.6 A and electrical frequency of 1.2 kHz.

In order to take into consideration the finite resolution of analog-to-digital converters (ADCs) and digital pulse width modulators (PWMs), the control scheme blocks of Figs. 3, 4, 5 and 6 have been discretized [$T_s = 50\,\mu s$ for PI, SMC and DPCC, $T_s = 25\,\mu s$ for MPC], measured currents and applied voltages have been quantized to 12 bits resolution while the rotor angle has been quantized considering a 20000 pulses per revolution.

All the simulations were carried out with the magnitude of the cogging torque T_c equal to 10% of the nominal torque.

A. CURRENT-LOOP BANDWIDTH

The current-loop bandwidth was computed at standstill and has been assessed for every different control strategy considering the current control loop only. At first, the simulations have been carried out considering the response to a sinusoidal reference current $i_q^\star$ with 0.6 A amplitude at different frequencies without saturating the applied output voltages.

An amplitude of 0.6 A has been chosen because with lower current values MPC applies the null vector and the reference cannot be followed. The same situation is exhibited in [27] with a FCS-MPC strategy for a H-Bridge driving an RL load.

Fig. 8 shows the response of the four strategies with a frequency of 1.2 kHz. It can be seen that the phase shift between $i_{q,DB}^\star$ and $i_{q,DB}$ approaches to 45 degrees (the same method is used in [28]), then the DPCC current-loop bandwidth value has been estimated to be approximately 1.2 kHz, while SMC and PI control follows the reference. In addiction, the MPC strategy shows a serious drawback when low currents are involved.

In Fig. 9 the PI and SMC current-loop bandwidth values have been estimated to be approximately 2.2 kHz, showing
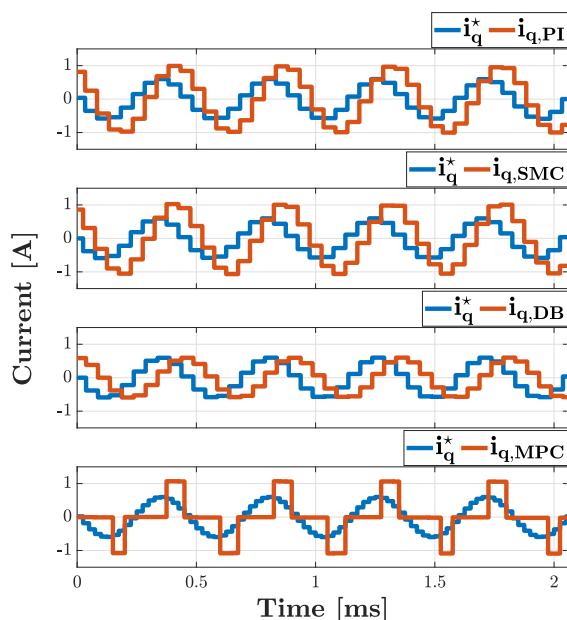
FIGURE 9. Response to a sinusoidal input with amplitude of 0.6 A and electrical frequency of 2.2 kHz.

FIGURE 10. Response to a sinusoidal input with amplitude of 3 A and electrical frequency of 1.5 kHz.

FIGURE 11. Response to a sinusoidal input with amplitude of 3 A and electrical frequency of 1.7 kHz.

a better response compared to DPCC control. The MPC response to a sinusoidal input current i_q with an amplitude of 0.6 A cannot be evaluated against the other strategies, since a greater current is needed to obtain an acceptable response. For this reason, the same test has also been assessed considering a sinusoidal input reference current with an amplitude of 3 A. In this condition the behaviour when the voltage saturates is studied.

Fig. 10 shows that the SMC control follows a reference with electrical frequency of 1.5 kHz, while the DPCC current-loop bandwidth has been estimated to be approximately 1.2 kHz, even if the reference amplitude is increased.

Fig. 11 shows that the PI control follows a reference with electrical frequency of 1.7 kHz. The worsening of the performance of the SMC and PI control strategies are due to the voltage saturation in the control loop. In this condition the MPC strategy is able to follow the reference showing a better response in terms of magnitude and phase shift compared to the other strategies. Lastly, Fig. 12 shows that MPC follows a reference with electrical frequency of approximately 2.3 kHz, showing a better response compared to the other strategies.

B. STEP RESPONSE ANALYSIS

In order to obtain additional information about the bandwidth, a step response analysis has been carried out as well.

Fig. 13 shows the response to a $i_q^\star$ current step between -0.6 A and 0.6 A, highlighting that the MPC strategy assures a faster response compared to the other control methods; even if a higher current ripple and distortion, due to the low input current, can be observed. In addiction, deadbeat control follows the reference in 2 sampling instants because the closed
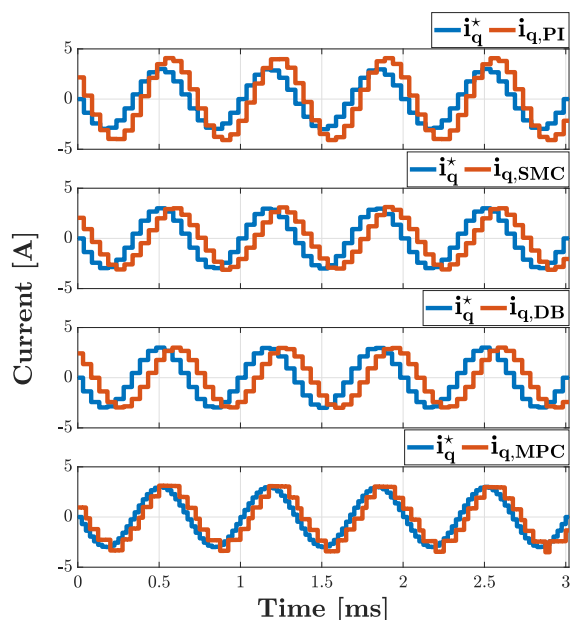
loop transfer function is equal to z^{-2}, as expected by the theoretical analysis. Since the MPC strategy shows a considerable steady state error when low input currents are involved, a step response analysis with a greater amplitude has been carried out.

Fig. 14 shows the response to a $i_q^\star$ current step between -5 A and 5 A, highlighting that the MPC strategy assure a faster response with respect to the other control methods,

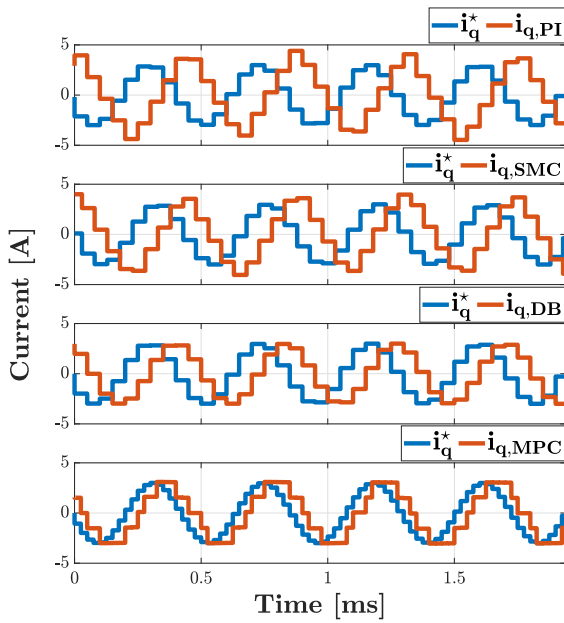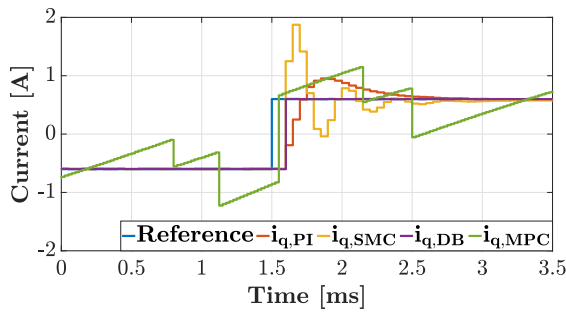**FIGURE 12.** Response to a sinusoidal input with amplitude of 3 A and electrical frequency of 2.3 kHz.

FIGURE 13. Response to a step between −0.6 A and 0.6 A.
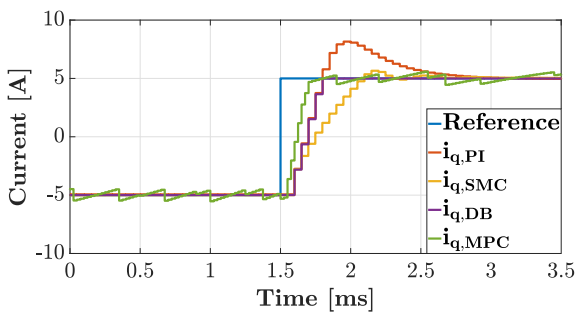

FIGURE 14. Response to a step between −5 A and 5 A.

while the response of the SMC strategy results to be the slowest. The step response of SMC can be faster acting on α, k_d and k_q in (11), although modifying these parameters to improve the step response lead to current oscillations which negatively affect the steady state error and the current loop bandwidth. For these reasons, SMC parameters have been

TABLE 3. Simulations. Control Strategies Rise Time to a Step Response

Control strategy	Current step [A]	Rise time [ms]
PI	[−0.6, 0.6]	0.1
	[−5, 5]	0.2
SMC	[−0.6, 0.6]	0.1
	[−5, 5]	0.5
DPCC	[−0.6, 0.6]	0
	[−5, 5]	0.2
MPC	[−0.6, 0.6]	0
	[−5, 5]	0.15

TABLE 4. Performance Comparison in Terms of RMS and THD

Control Strategy	Stator Current	$T_L = 1\,\text{Nm}$		$T_L = 4\,\text{Nm}$	
		THD (%)	RMS [A]	THD (%)	RMS [A]
PI	i_α	5.28	1.10	1.68	4.39
SMC	i_α	5.13	1.10	1.51	4.39
DPCC	i_α	5.41	1.10	2.09	4.39
MPC	i_α	21.17	1.12	5.42	4.39

tuned to obtain a trade off in order to maximise the current-loop bandwidth while ensuring low current oscillations.

In this condition, DPCC requires more than 2 sampling instants because the response is limited by the maximum voltage available. After the transient, the steady state condition is well regulated without error.

In Table 3 results in terms of rise time are summarized for the simulation of Fig. 13 and Fig. 14.

C. SPEED-LOOP ANALYSIS

In order to evaluate the root mean square value (RMS) and the total harmonic distortion (THD) of the phase currents for the different control strategies, a speed-loop analysis has been carried out. The speed loop is closed on a PI regulator whose proportional and integral gains have been chosen while simulating the PI control strategy and they have been left unchanged for the other topologies. In order to compare the results of the four strategies, the PI regulator closed on the speed-loop of the MPC has been discretized with the same sampling period used for the other topologies. The simulations have been carried out imposing a reference constant speed of 40 rad/s, well below the flux-weakening operative region. At first, the THD and RMS value of the phase current i_a are evaluated when a load torque of 1 Nm is imposed. Then, the same analysis is repeated imposing a load torque of 4 Nm. The results obtained for i_a are the same as the phase current i_b. Table 4 summarizes the results in terms of THD and RMS. It can be noted that with low currents MPC has much more THD compared to the other strategies. When high currents are involved, the THD of MPC strategy reduces considerably even if it is sill higher with respect to the other strategies.

V. EXPERIMENTAL RESULTS
The proposed control schemes have been finally tested by experiments. The controllers are implemented in their discrete version on a commercial STM32H743ZI DSP controller. The DSP is used to implement the proposed controls, as well as
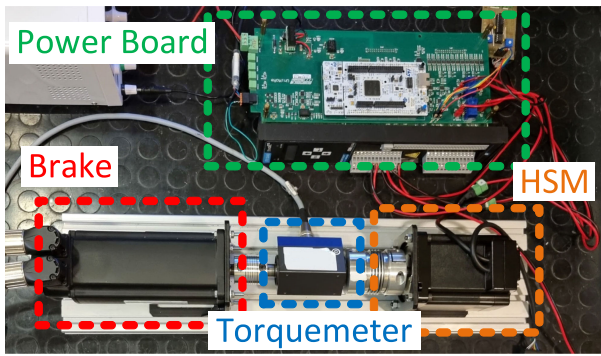
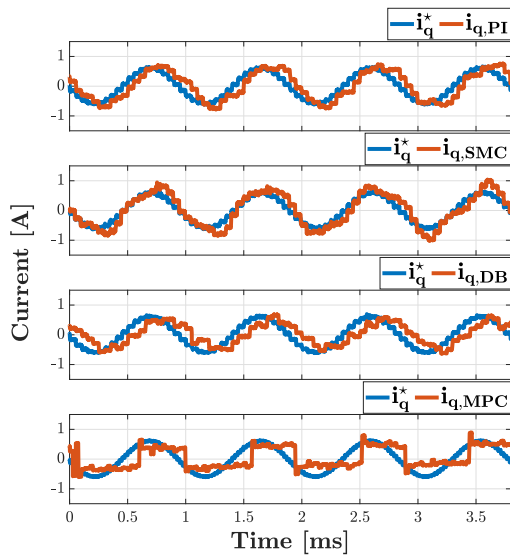**FIGURE 15.** Test bench with HSM, brake, torquemeter and power board.

FIGURE 16. Response to a sinusoidal input with amplitude of 0.6 A and electrical frequency of 1 kHz.

FIGURE 17. Response to a sinusoidal input with amplitude of 0.6 A and electrical frequency of 1.5 kHz.
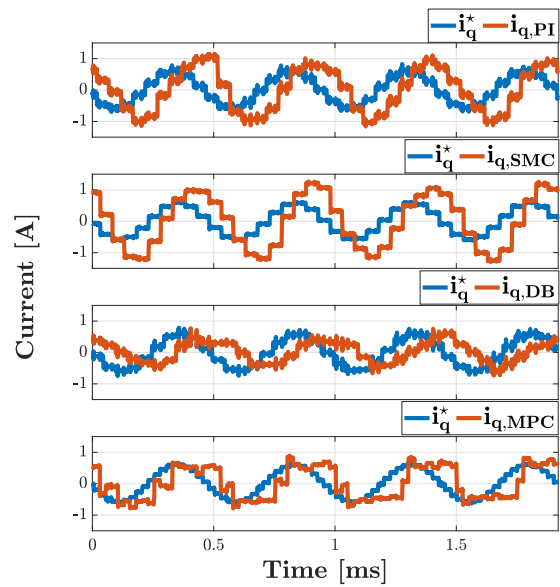
FIGURE 18. Response to a sinusoidal input with amplitude of 0.6 A and electrical frequency of 2.2 kHz.

to generate the PWM signals and to acquire the two motor phase currents. The hybrid stepper motor AM34SS3DGA-N is a two-phase salient stepper motor with 50 rotor teeth and a step angle of 1.8° employing an incremental encoder with 20000 counts/rev.

The HSM is installed on the test bench shown in Fig. 15 which also includes a torquemeter and a brushless machine as brake.

A. CURRENT-LOOP BANDWIDTH

The current-loop bandwidth was computed at standstill in the same manner as the simulations, i.e. with sinusoidal i_q^* current reference. Experimental data are extracted from the test bench of Fig. 15 and processed with Matlab for visualization purpose.

Fig. 16 shows the response of the four strategies with a frequency of 1 kHz. The DPCC current-loop bandwidth value has been estimated to be approximately 1 kHz (the phase difference is approximately 45 degrees), while SMC and PI
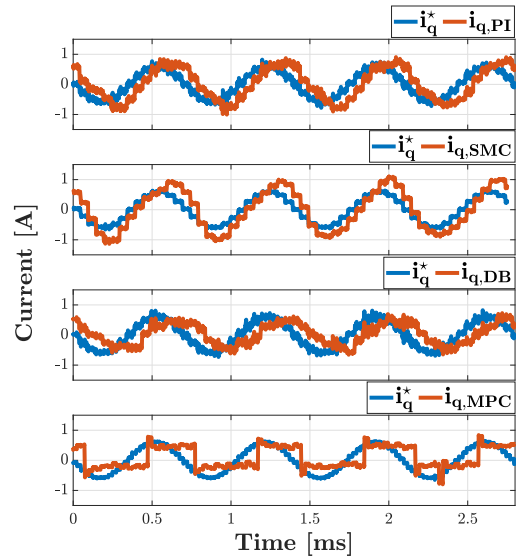
controls track the reference with smaller angle delay. As expected, in this condition MPC shows serious drawback to work with low currents.

In Fig. 17 the PI current-loop bandwidth value has been estimated to be approximately 1.5 kHz, showing a better response with respect to DPCC control, as expected.

In Fig. 18 the SMC current-loop bandwidth value has been estimated to be approximately 2.2 kHz showing the same result that has been achieved in simulation.

In the same way as in the simulations, the response of the different control strategies has also been assessed considering a sinusoidal input reference current with an amplitude of 3 A,
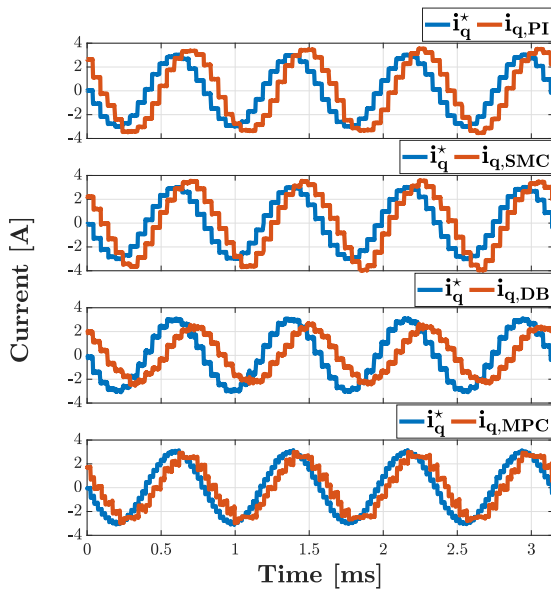
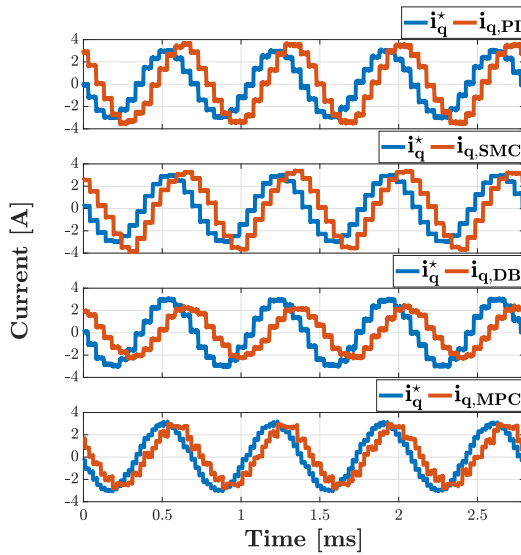**FIGURE 19.** Response to a sinusoidal input with amplitude of 3 A and electrical frequency of 1.2 kHz.

FIGURE 20. Response to a sinusoidal input with amplitude of 3 A and electrical frequency of 1.5 kHz.

FIGURE 21. Response to a sinusoidal input with amplitude of 3 A and electrical frequency of 2 kHz.

FIGURE 22. Response to a step between −0.6 A and 0.6 A.

Lastly, in Fig. 21 the MPC current-loop follows a reference of approximately 2 kHz, showing a better response with respect to the other strategies.

B. STEP RESPONSE ANALYSIS

In this subsection the response to a step input has been carried out in the same manner as the simulations.

Fig. 22 shows the response to a $i_q^\star$ current step between −0.6 A and 0.6 A. The SMC, PI and DPCC controls shows a similar transient response, while the MPC strategy response shows a high current ripple and a remarkable distortion due to the low input current, as expected from the simulations. In order to better evaluate the MPC strategy, a step response analysis with a greater amplitude has been carried out.

Fig. 23 shows the response to a $i_q^\star$ current step between −5 A and 5 A, highlighting that the MPC strategy assure a faster response with respect to the other control methods. Concerning the simulations, the PI control strategy shows a faster response than the DPCC control strategy, while the SMC response is the slowest as expected. As stated in [29], a predictive current control method is based on nominal parameters in order to predict and control the current of the motor,

in this last case the saturation of the output voltages happens during transients.

Fig. 19 shows that SMC and PI control follows a reference of approximately 1.2 kHz. Increasing the amplitude of the current reference, the DPCC has the same bandwidth of Fig. 16. In fact, when a reference of 1.2 kHz is followed as in Fig. 19, DPCC exhibits a phase delay more than 45 degrees respect to the reference. As expected, in this condition the MPC is able to follow the reference showing a better response in terms of magnitude and phase shift compared to the other strategies.

In the same way as the simulation, Fig. 20 shows that the SMC strategy follows a reference of approximately 1.5 kHz.
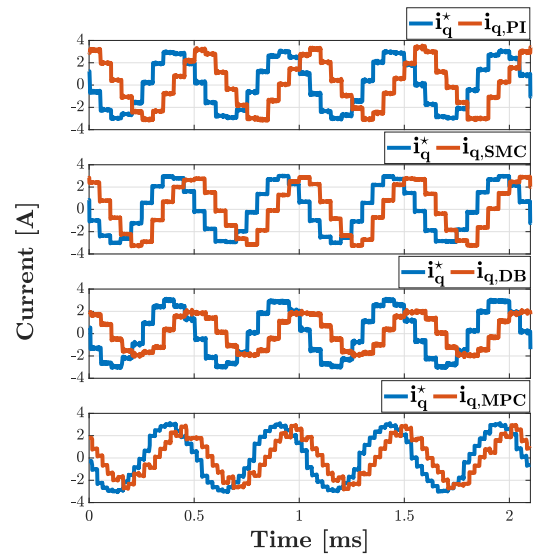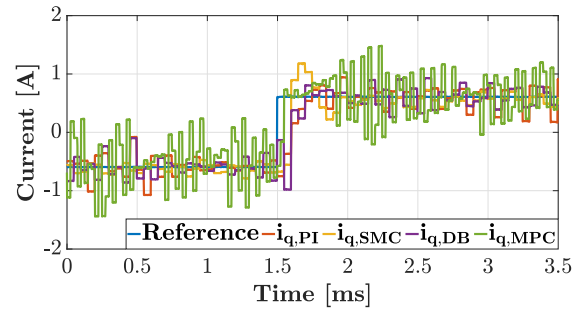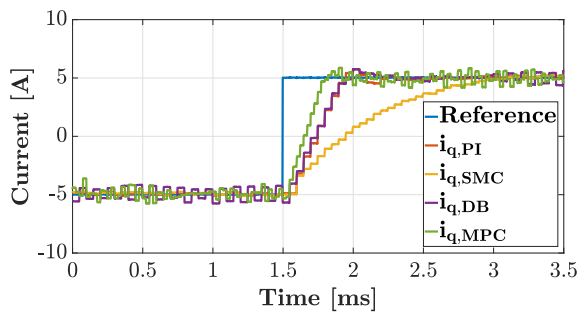
FIGURE 23. Response to a step between −5 A and 5 A.

TABLE 5. Experiments. Control Strategies Rise Time to a Step Response

Control Strategy	Current Step [A]	Rise Time [ms]
PI	[-0.6, 0.6]	0.05
	[-5, 5]	0.3
SMC	[-0.6, 0.6]	0
	[-5, 5]	1.1
DPCC	[-0.6, 0.6]	0.05
	[-5, 5]	0.3
MPC	[-0.6, 0.6]	0
	[-5, 5]	0.225

TABLE 6. Experiments. Performance Comparison in Terms of RMS and THD

Control Strategy	Stator Current	$T_L = 1\,\mathrm{Nm}$		$T_L = 4\,\mathrm{Nm}$	
		THD (%)	RMS [A]	THD (%)	RMS [A]
PI	i_α	7.74	1.59	5.28	5.28
SMC	i_α	7.67	1.56	5.21	5.28
DPCC	i_α	7.47	1.51	5.73	5.28
MPC	i_α	28.75	1.46	8.33	5.28

so a mismatch between actual parameters and their nominal values can appear due to temperature rise (which has effect on R_s and k_M) or magnetic saturation (which has effect on L_0). The DPCC control strategy seems to suffer parameter mismatches much more than the MPC strategy.

In Table 5 results in terms of rise time are summarized for the experimentals of Fig. 22 and Fig. 23.

C. SPEED LOOP ANALYSIS

The speed-loop analysis was computed in the same manner as the simulations. Table 4 summarizes the results in terms THD and RMS. While PI, SMC and DPCC show similar results and are comparable, it can be noted that with low currents MPC has a higher THD compared to the other strategies, while with high currents the THD tends to decrease as expected from the simulations.

D. COMPUTATIONAL COST

The computational cost of the four strategies is compared based on the execution times when the control is closed on the speed loop. The algorithms runs with an internal clock of 480 MHz and results are summarized in Table 7.

TABLE 7. Computational Cost of Implemented Strategies

Strategy	Computational cost [μs]
PI	5.6
SMC	5.8
DPCC	5.4
MPC	17.8

Due to the evaluation of every possible configuration the MPC execution time is bigger, while the other strategies highlight similar behaviours.

VI. CONCLUSION

This paper analyzes the performance of different current control strategies for a HSM in terms of current loop bandwidth and THD of the phase currents. While PI, SMC and DPCC control strategies show a better behaviour than the MPC strategy in terms of bandwidth when low currents are involved, as the amplitude current increases the MPC strategy provides higher bandwidth and faster step response. In terms of THD, PI, SMC and DPCC have similar behaviour with low and high currents, while MPC tends to work better when higher currents are involved.

REFERENCES

[1] K. M. Le, H. Van Hoang, and J. W. Jeon, "An advanced closed-loop control to improve the performance of hybrid stepper motors," *IEEE Trans. Power Electron.*, vol. 32, no. 9, pp. 7244–7255, Sep. 2017.

[2] S. Derammelaere *et al.*, "The efficiency of hybrid stepping motors: Analyzing the impact of control algorithms," *IEEE Ind. Appl. Mag.*, vol. 20, no. 4, pp. 50–60, Jul./Aug. 2014.

[3] V. Salis *et al.*, "Learning position controls for hybrid step motors: From current-fed to full-order models," *IEEE Trans. Ind. Electron.*, vol. 65, no. 8, pp. 6120–6130, Aug. 2018.

[4] A. Arias, J. Caum, E. Ibarra, and R. Griñó, "Reducing the cogging torque effects in hybrid stepper machines by means of resonant controllers," *IEEE Trans. Ind. Electron.*, vol. 66, no. 4, pp. 2603–2612, Apr. 2019.

[5] S.-K. Kim and C. K. Ahn, "Position regulator with variable cut-off frequency mechanism for hybrid-type stepper motors," *IEEE Trans. Circuits Syst. I, Reg. Papers*, vol. 67, no. 10, pp. 3533–3540, Oct. 2020.

[6] S.-H. Chang, P.-Y. Chen, Y.-H. Ting, and S.-W. Hung, "Robust current control-based sliding mode control with simple uncertainties estimation in permanent magnet synchronous motor drive systems," *IET Electric Power Appl.*, vol. 4, no. 6, pp. 441–450, Jul. 2010.

[7] X. Zhang and X. Huang, "An incremental deadbeat predictive current control method for PMSM with low sensitivity to parameter variation," in *Proc. Int. Conf. Elect. Mach.*, 2020, vol. 1, pp. 1060–1066.

[8] S. Walz, R. Lazar, G. Buticchi, and M. Liserre, "Dahlin-based fast and robust current control of a PMSM in case of low carrier ratio," *IEEE Access*, vol. 7, pp. 102199–102208, 2019.

[9] J. Rodriguez and P. Cortes, *Predictive Control of Power Converters and Electrical Drives*. Hoboken, NJ, USA: Wiley, 2012.

[10] X. Yuan, S. Zhang, C. Zhang, A. Galassini, G. Buticchi, and M. Degano, "Improved model predictive current control for SPMSM drives using current update mechanism," *IEEE Trans. Ind. Electron.*, vol. 68, no. 3, pp. 1938–1948, Mar. 2021.

[11] J. Falck, G. Buticchi, and M. Liserre, "Thermal stress based model predictive control of electric drives," *IEEE Trans. Ind. Appl.*, vol. 54, no. 2, pp. 1513–1522, Mar./Apr. 2018.

[12] C. R. Baier, R. O. Ramirez, E. I. Marciel, J. C. Hernández, P. E. Melín, and E. E. Espinosa, "FCS-MPC without steady-state error applied to a grid-connected cascaded H-bridge multilevel inverter," *IEEE Trans. Power Electron.*, vol. 36, no. 10, pp. 11785–11799, Oct. 2021.

[13] M. Bendjedia, Y. Ait-Amirat, B. Walther, and A. Berthon, "Position control of a sensorless stepper motor," *IEEE Trans. Power Electron.*, vol. 27, no. 2, pp. 578–587, Feb. 2012.

[14] N. Matsui, M. Nakamura, and T. Kosaka, "Instantaneous torque analysis of hybrid stepping motor," *IEEE Trans. Ind. Appl.*, vol. 32, no. 5, pp. 1176–1182, Sep./Oct. 1996.

[15] B.-H. Bae and S.-K. Sul, "A compensation method for time delay of full-digital synchronous frame current regulator of PWM AC drives," *IEEE Trans. Ind. Appl.*, vol. 39, no. 3, pp. 802–810, May/Jun. 2003.

[16] A. Visioli, *Practical PID Control*. London, U.K.: Springer, 2006.

[17] Y. Wang, Y. Feng, X. Zhang, and J. Liang, "A new reaching law for antidisturbance sliding-mode control of PMSM speed regulation system," *IEEE Trans. Power Electron.*, vol. 35, no. 4, pp. 4117–4126, Apr. 2020.

[18] H. Kim, J. Son, and J. Lee, "A high-speed sliding-mode observer for the sensorless speed control of a PMSM," *IEEE Trans. Ind. Electron.*, vol. 58, no. 9, pp. 4069–4077, Sep. 2011.

[19] G. Liu, H. Zhang, and X. Song, "Position-estimation deviation-suppression technology of PMSM combining phase self-compensation SMO and feed-forward PLL," *IEEE Trans. Emerg. Sel. Topics Power Electron.*, vol. 9, no. 1, pp. 335–344, Feb. 2021.

[20] X. Yu, Y. Feng, and Z. Man, "Terminal sliding mode control – an overview," *IEEE Open J. Ind. Electron. Soc.*, vol. 2, pp. 36–52, 2021, doi: 10.1109/OJIES.2020.3040412.

[21] V. Utkin, J. Guldner, and J. Shi, *Sliding Mode Control in Electro-Mechanical Systems*. Philadelphia, PA, USA: CRC Press, 2017.

[22] L. Springob and J. Holtz, "High-bandwidth current control for torque-ripple compensation in PM synchronous machines," *IEEE Trans. Ind. Electron.*, vol. 45, no. 5, pp. 713–721, Oct. 1998.

[23] M. Yang, X. Lang, J. Long, and D. Xu, "Flux immunity robust predictive current control with incremental model and extended state observer for PMSM drive," *IEEE Trans. Power Electron.*, vol. 32, no. 12, pp. 9267–9279, Dec. 2017.

[24] X. Zhang, L. Zhang, and Y. Zhang, "Model predictive current control for PMSM drives with parameter robustness improvement," *IEEE Trans. Power Electron.*, vol. 34, no. 2, pp. 1645–1657, Feb. 2019.

[25] P. Cortes, J. Rodriguez, C. Silva, and A. Flores, "Delay compensation in model predictive current control of a three-phase inverter," *IEEE Trans. Ind. Electron.*, vol. 59, no. 2, pp. 1323–1325, Feb. 2012.

[26] V. Yaramasu and B. Wu, *Model Predictive Control of Wind Energy Conversion Systems*. New York, NY, USA: Wiley, 2016.

[27] R. P. Aguilera, P. Lezana, and D. E. Quevedo, "Finite-control-Set model predictive control with improved steady-state performance," *IEEE Trans. Ind. Informat.*, vol. 9, no. 2, pp. 658–667, May 2013.

[28] H. Kim, M. W. Degner, J. M. Guerrero, F. Briz, and R. D. Lorenz, "Discrete-time current regulator design for AC machine drives," *IEEE Trans. Ind. Appl.*, vol. 46, no. 4, pp. 1425–1435, Jul./Aug. 2010.

[29] Y. Li, Y. Li, and Q. Wang, "Robust predictive current control with parallel compensation terms against multi-parameter mismatches for PMSMs," *IEEE Trans. Energy Convers.*, vol. 35, no. 4, pp. 2222–2230, Dec. 2020.

EMILIO CARFAGNA (Student Member, IEEE) was born in Frosinone, Italy, in 1992. He received the master's degree in automation engineering from the University of Rome Tor Vergata, Rome, Italy, in 2018, and the Ph.D. degree from the University of Modena and Reggio Emilia, Modena, Italy, in 2022. He is currently a Research Fellow with Electric Drives and Power Electronics Group, University of Modena and Reggio Emilia, Modena, Italy. In 2021, he joined the Chair of Power Electronics, Kiel, Germany, as a Visiting Scholar. His research interests mainly include sensorless control design for electrical drives and industrial applications.

GIOVANNI MIGLIAZZA (Member, IEEE) received the master's degree in mechatronic engineering and the Ph.D. degree in industrial innovation engineering from the University of Modena and Reggio Emilia, Modena, Italy, in 2014 and 2020, respectively. He is currently a Researcher with the University of Modena and Reggio Emilia. He also worked as a Senior Research Fellow with the University of Nottingham, Ningbo, China. He has authored or coauthored more than 25 scientific papers and has received one industrial patent. His research interests include power electronics, converters, and electric drives. He is currently a Member of the IEEE-IES Technical Committee on Renewable Energy Systems. He constantly serves the scientific community as a Reviewer for several journals and conferences.

GIAMPAOLO BUTICCHI (Senior Member, IEEE) received the master's degree in electronic engineering and the Ph.D. degree in information technologies from the University of Parma, Parma, Italy, in 2009 and 2013, respectively. In 2012, he was a Visiting Researcher with the University of Nottingham, Nottingham, U.K. Between 2014 and 2017, he was a Postdoctoral Researcher and Guest Professor with the University of Kiel, Kiel, Germany. In 2017, he was appointed as an Associate Professor with The University of Nottingham, Ningbo, China, and the Head of Power Electronics with Nottingham Electrification Center. In 2020, he was promoted to Professor. He is the author or coauthor of more than 260 scientific papers. His research interests include power electronics for renewable energy systems, smart transformer fed microgrids and dc grids for the More Electric Aircraft. Dr. Buticchi is involved in the major international organizations (IEEE, IET, RAeS, and HEA) and has been organizing tutorials and special sessions in the relevant conferences and journals related to power electronics. He is an Associate Editor for the IEEE TRANSACTIONS ON INDUSTRIAL ELECTRONICS, IEEE TRANSACTIONS ON TRANSPORTATION ELECTRIFICATION, and IEEE Open Journal of the Industrial Electronics Society. He is currently the Chair of the IEEE Industrial Electronics Society Technical Committee on Renewable Energy Systems and Cluster Delegate. During his stay in Germany, he was the recipient of Von Humboldt Postdoctoral Fellowship to carry out research related to fault tolerant topologies of smart transformers.

FABIO BERNARDI (Student Member, IEEE) was born in Modena, Italy, in 1992. He received the master's degree in mechatronic engineering in 2020 from the University of Modena and Reggio Emilia, Modena, Italy, where he is currently working toward the Ph.D. degree. His main research interests include power electronics, electric drives, and converters.

FABIO IMMOVILLI (Senior Member, IEEE) received the M.S. degree and the Ph.D. degree in mechatronic engineering with the University of Modena and Reggio Emilia, Modena, Italy, in 2006 and 2011, respectively. Since November 2019, he has been an Associate Professor of electric converters, machines and drives with the Department of Sciences and Methods for Engineering, University of Modena and Reggio Emilia. He is the author or coauthor of more than 55 technical papers. His current research interests include electric machine condition monitoring, electric power converters, machines for energy conversion from renewable energy sources, and thermoacoustics.

EMILIO LORENZANI (Senior Member, IEEE) received the M.S. degree in electronic engineering and the Ph.D. degree in information technologies from the University of Parma, Parma, Italy, in 2002 and 2006, respectively. Since 2011, he has been with the Department of Science and Engineering Methods, University of Modena and Reggio Emilia, Modena, Italy, where he is currently an Associate Professor of electric machines and drives. He is the author or coauthor of more than 80 technical papers. He holds five industrial patentsHis research interests include power electronics for renewable energy resources, electric drives, and electric motor diagnostics. Dr. Lorenzani is an Associate Editor for *IET Power Electronics*.